Seeding Atomic Layer Deposition of High-*k* Dielectrics on Epitaxial Graphene with Organic Self-Assembled Monolayers

Justice M. P. Alaboson,[†,‡] Qing Hua Wang,[†,#] Jonathan D. Emery,[†] Albert L. Lipson,[†] Michael J. Bedzyk,[†,‡,§] Jeffrey W. Elam,[⊥] Michael J. Pellin,[‡,∥] and Mark C. Hersam[†,∥,¶,*]

[†]Department of Materials Science and Engineering, Northwestern University, Evanston, Illinois 60208, United States, [‡]Materials Science Division, Argonne National Laboratory, Argonne, Illinois 60439, United States, [§]Department of Physics and Astronomy, Northwestern University, Evanston, Illinois 60208, United States, [⊥]Energy Systems Division, Argonne National Laboratory, Argonne, Illinois 60439, United States, and [∥]Department of Chemistry and [¶]Department of Medicine, Northwestern University, Evanston, Illinois 60208, United States. [#]Present address: Department of Chemical Engineering, Massachusetts Institute of Technology, Cambridge, Massachusetts 02139.

ABSTRACT The development of high-performance graphene-based nanoelectronics requires the integration of ultrathin and pinhole-free high-*k* dielectric films with graphene at the wafer scale. Here, we demonstrate that self-assembled monolayers of perylene-3,4,9,10-tetracarboxylic dianhydride (PTCDA) act as effective organic seeding layers for atomic layer deposition (ALD) of HfO_2 and Al_2O_3 on epitaxial graphene on SiC(0001). The PTCDA is deposited *via* sublimation in ultrahigh vacuum and shown to be highly ordered with low defect density by molecular-resolution scanning tunneling microscopy. Whereas identical ALD conditions lead to incomplete and rough dielectric deposition on bare graphene, the chemical functionality provided by the PTCDA seeding layer yields highly uniform and conformal films. The morphology and chemistry of the dielectric films are characterized by atomic force microscopy, ellipsometry, cross-sectional scanning electron microscopy, and X-ray photoelectron spectroscopy, while high-resolution X-ray reflectivity measurements indicate that the underlying graphene remains intact following ALD. Using the PTCDA seeding layer, metal-oxide-graphene capacitors fabricated with a 3 nm Al_2O_3 and 10 nm HfO_2 dielectric stack show high capacitance values of $\sim$700 nF/cm^2 and low leakage currents of $\sim 5 \times 10^{-9}$ A/cm^2 at 1 V applied bias. These results demonstrate the viability of sublimated organic self-assembled monolayers as seeding layers for high-*k* dielectric films in graphene-based nanoelectronics.

KEYWORDS: graphene · gate insulator · transistor · hafnia · alumina · PTCDA · organic seeding layer

The outstanding electronic transport properties of graphene, including extremely high carrier mobilities, have generated significant interest in graphene-based nanoelectronics.[1−3] An important step in the development of top-gated graphene-based field-effect transistors (FETs) is the growth of high dielectric constant (high-*k*) materials to act as the gate insulator. For optimal performance, these dielectric thin films should be ultrathin, conformal, and pinhole-free with minimal disorder or traps at the dielectric−graphene interface. However, due to the chemical inertness and hydrophobicity of graphene, the direct growth or deposition of dielectric layers on bare graphene leads to non-uniform films[4,5] with sub-optimal electrical performance.

Several surface treatment strategies have been pursued by researchers to improve the uniformity of gate dielectric growth on graphene by atomic layer deposition (ALD), including the deposition and oxidation of metal films,[6−11] functionalization of graphene *via* ozone[12,13] and nitrogen dioxide,[14] and the spin-coating of polymer films as seeding layers.[15,16] Although these methods possess clear advantages compared to ALD dielectric deposition directly on pristine graphene, important issues remain unresolved.[17] For example, graphene surface pretreatments that involve oxidized metal nucleation layers, ozone, or nitrogen dioxide generally lead to surface damage of the graphene and degradation of its electronic properties.[8,14] Furthermore, polymer seeding layers decrease the overall capacitance of the gate dielectric layer due to increased gate thickness and a reduced effective *k* value.[15,16] Additional solution-phase deposited organic seeding layers have also been explored, although the electrical properties of the resulting ALD alumina have not been reported.[4] Consequently, a clear need remains for a graphene chemical functionalization scheme that efficiently and uniformly seeds ALD growth while preserving the underlying graphene structure and achieving desirable dielectric properties such as low leakage current and high capacitance.

* Address correspondence to m-hersam@northwestern.edu.

Received for review April 18, 2011 and accepted May 9, 2011.

Published online May 09, 2011
10.1021/nn201414d

Herein, we demonstrate an alternative ALD seeding layer based on organic monolayers of perylene-3,4,9,10-tetracarboxylic dianhydride (PTCDA) that overcomes the aforementioned issues for high-*k* dielectric thin films on epitaxial graphene (EG) on SiC(0001). PTCDA is deposited *via* gas-phase sublimation in ultrahigh vacuum (UHV),[18,19] resulting in a highly uniform and ordered self-assembled monolayer as verified with UHV scanning tunneling microscopy (STM). Subsequent ALD yields homogeneous and conformal thin films of Al_2O_3 and HfO_2 whose structure and chemistry are characterized with atomic force microscopy (AFM), ellipsometry, X-ray photoelectron spectroscopy (XPS), cross-sectional scanning electron microscopy (SEM), and low-angle and high-angle X-ray reflectivity (XRR). As a subsurface probe, XRR also allows verification of the structural integrity of the underlying graphene following ALD dielectric growth. Finally, metal-oxide-graphene capacitors are fabricated *via* PTCDA-seeded ALD of a 3 nm Al_2O_3 and 10 nm HfO_2 dielectric stack, resulting in a measured capacitance of $\sim$700 nF/cm^2 and leakage current of $\sim 5 \times 10^{-9}$ A/cm^2 at 1 V gate bias. Overall, this work reveals the effectiveness of sublimated organic monolayers as seeding layers for ALD on EG, thus facilitating the development of graphene-based nanoelectronic devices and circuits.

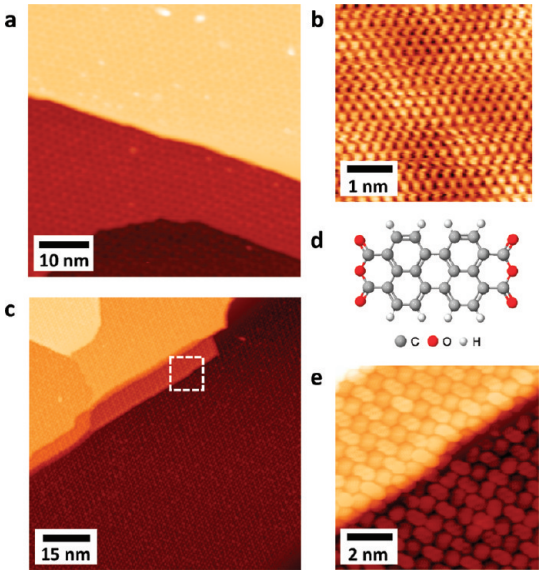

Figure 1. (a) STM image of the epitaxial graphene surface prepared by UHV graphitization of SiC(0001) (imaging conditions: sample voltage $V_s = -2.0$ V, tunneling current $I_t = 0.05$ nA). (b) Atomically resolved bilayer graphene ($V_s = -0.3$ V, $I_t = 0.1$ nA). (c) Large-area STM image of PTCDA monolayer, which conformally coats several step edges in a uniform ordered monolayer ($V_s = -2.0$ V, $I_t = 0.05$ nA). (d) Molecular structure of PTCDA. (e) High-resolution STM image of the area marked by the square in (c), showing the herringbone arrangement of the PTCDA molecules and continuous ordering over a substrate step edge ($V_s = -2.0$ V, $I_t = 0.07$ nA).

RESULTS AND DISCUSSION

UHV STM of PTCDA Monolayers. Graphene was epitaxially grown on n-type 6H-SiC(0001) substrates (Cree, Inc.) by UHV graphitization as described previously,[18,20,21] resulting in a mixture of monolayer and bilayer graphene. Atomic-scale characterization was accomplished in the same UHV system using a home-built STM at room temperature.[22] A large-area STM image of the bare epitaxial graphene surface is shown in Figure 1a, and an atomically resolved STM image of bilayer graphene is included in Figure 1b. Following STM confirmation of successful epitaxial graphene growth, the PTCDA monolayer was formed by sublimating PTCDA (97%, Sigma-Aldrich) onto the graphene surface at room temperature in UHV following a previously established protocol.[18] The molecules self-assemble into a well-ordered monolayer that homogeneously and conformally coats the graphene surface, as shown in the STM image of Figure 1c. The molecular structure of PTCDA is illustrated in Figure 1d. The central perylene core of PTCDA induces the molecule to lay flat on the graphene surface *via* $\pi-\pi^*$ stacking, while the oxygenated periphery of the molecule provides relatively strong noncovalent intermolecular bonding that stabilizes the monolayer[18] and also possesses distinct chemical character from the underlying graphene that holds promise for templating subsequent chemistry such as ALD. In the molecularly resolved STM image of Figure 1e, the monolayer shows a highly ordered herringbone structure. In addition, the ordering of the monolayer is unperturbed by underlying substrate defects such as atomic step edges.[18] Overall, PTCDA deposition results in a structurally and chemically homogeneous surface with a lower defect density than the original bare graphene.

Structural and Chemical Characterization of ALD Dielectric Films. Representative intermittent contact AFM images of EG and PTCDA/EG surfaces are presented in Figure 2a,d, respectively. ALD of Al_2O_3 and HfO_2 was then performed in a custom viscous flow ALD reactor[23] at a growth temperature of 100 °C. Figure 2b,c shows AFM images of two EG surfaces after depositing 25 cycles of Al_2O_3 and 25 cycles of HfO_2, respectively. The high-*k* dielectric films on the bare EG surface are patchy and discontinuous, which confirms previous reports of ALD on nonfunctionalized graphene and HOPG surfaces.[4,5,10] In contrast, Figure 2e,f shows AFM images of two PTCDA/EG surfaces following the same ALD treatment as EG (*i.e.*, 25 cycles of Al_2O_3 and 25 cycles of HfO_2, respectively). With the PTCDA seeding layer, the resulting ALD dielectric films possess high uniformity, low defect density, and appear to conformally coat the underlying terraces of the EG surface as evidenced by the presence of atomic steps in the post-ALD AFM images. Quantitatively, the measured rms roughness of both films on PTCDA/EG is less than 0.3 nm. This superlative uniformity, conformality, and smoothness

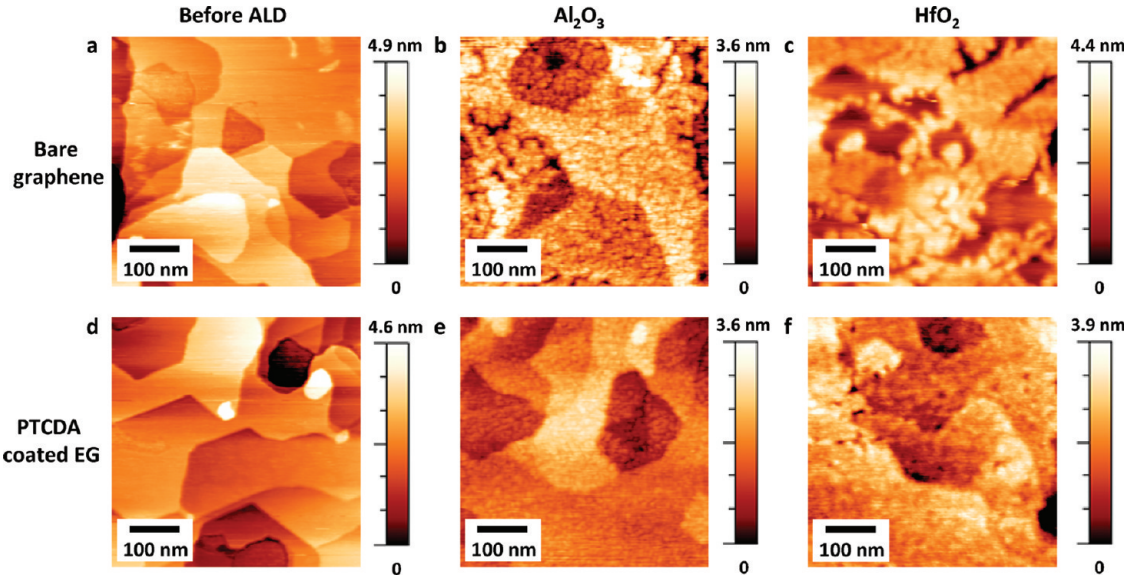

Figure 2. (a) Representative AFM image of an epitaxial graphene surface prepared by UHV graphitization. (b,c) AFM images of a bare epitaxial graphene surface after ALD of (b) 25 cycles of Al_2O_3 and (c) 25 cycles of HfO_2. (d–f) AFM images of a PTCDA-functionalized epitaxial graphene surface (d) immediately after PTCDA deposition, and following ALD of (e) 25 cycles of Al_2O_3 and (f) 25 cycles of HfO_2. All AFM images were taken in intermittent contact mode.

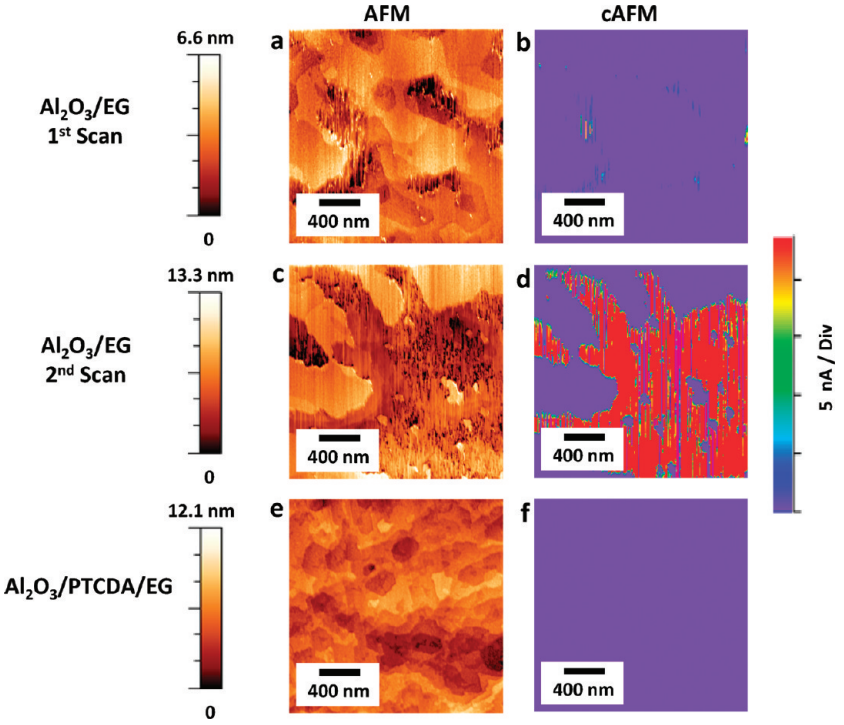

Figure 3. (a,b) Initial conductive AFM (cAFM) scan showing (a) topography and (b) current image of an EG surface after 25 cycles of Al_2O_3 ALD. (c,d) Second AFM scan showing (c) topography and (d) current image of the same region as (a,b). (e) Topography and (f) current image of a PTCDA/EG surface after 25 ALD cycles of Al_2O_3. All of these images were taken in contact mode using a conductive diamond-coated Si probe (CDT-FMR, Nanosensors). Current maps were taken at a sample bias of 0.3 V using an inline 12 MΩ limiting resistor. The AFM imaging set point was 20 nN.

of the dielectric films persist even following extended ALD treatments that yield thin films with thicknesses above 15 nm.

To probe the adhesion between the deposited ALD films and the underlying substrate, contact-mode conductive AFM imaging was employed. Figure 3a–d shows that after only one AFM scan in contact mode (contact force ~ 20 nN) defects are introduced in the Al_2O_3 (25 cycles ALD) dielectric film on bare EG; while after just two AFM scans, large regions of the dielectric film are removed, exposing the underlying electrically conductive EG/SiC substrate. On the other hand,

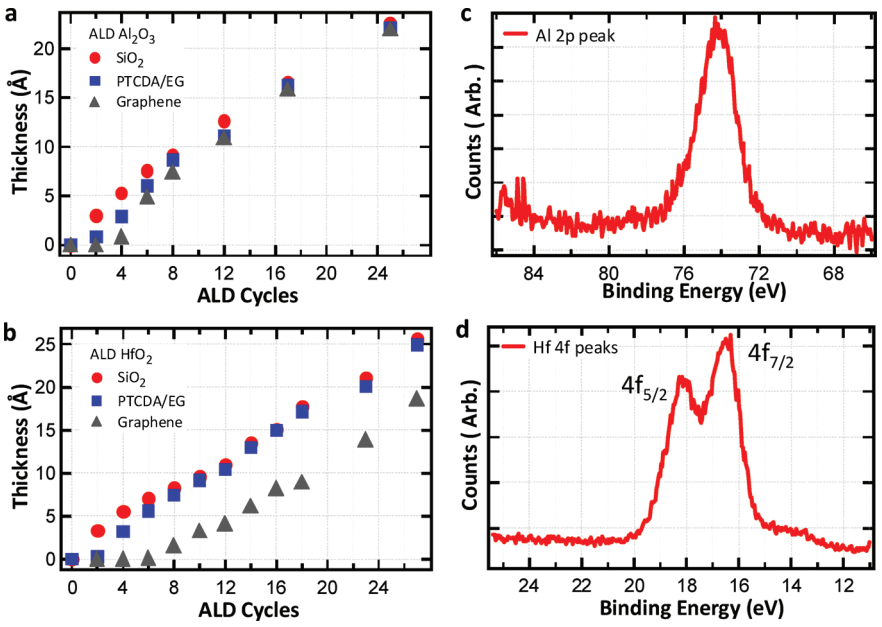

Figure 4. (a) Plot of Al_2O_3 thickness as a function of ALD cycles for SiO_2, PTCDA/EG, and bare EG. (b) Plot of HfO_2 thickness as a function of ALD cycles for SiO_2, PTCDA/EG, and bare EG. Compared to SiO_2 and PTCDA/EG, ALD growth on EG is initially inhibited due to the lack of reactive sites. (c) Al 2p peak in the XPS spectra of (25 cycles) Al_2O_3/PTCDA/EG. The Al 2p peak position at ~74.2 eV indicates the presence of Al_2O_3. (d) Hf $4f_{5/2}$ and Hf $4f_{7/2}$ peaks in the XPS spectra of (25 cycles) HfO_2/PTCDA/EG. The Hf $4f_{7/2}$ peak position at ~16.5 eV indicates the presence of HfO_2.

Figure 3e,f shows that the Al_2O_3 (25 cycles ALD) dielectric film on PTCDA/EG is unchanged by contact-mode AFM even following multiple AFM scans at contact forces up to 50 nN. The stability of the Al_2O_3 film on PTCDA/EG following contact-mode imaging indicates strong adhesion of the dielectric film. In addition, the absence of detectable current in the conductive AFM current map of Figure 3f suggests that the dielectric film on PTCDA/EG is uniformly electrically insulating.

The thickness and chemistry of the ALD dielectric films were determined by ellipsometry and XPS, respectively. In particular, ellipsometric measurements were obtained before and after ALD using a J.A. Woolam Co. M2000 V variable angle spectroscopic ellipsometer (VASE). The thicknesses of the Al_2O_3 and HfO_2 dielectric films were obtained by fitting the ellipsometric data to a model using known optical constants of the dielectric films and the contribution from the substrate obtained preceding ALD. Figure 4a,b contains plots of the ellipsometrically determined dielectric film thickness as a function of ALD growth cycle number for Al_2O_3 and HfO_2, respectively. Figure 4a shows that the Al_2O_3 ALD on the bare EG surface is initially inhibited for ~3−4 ALD cycles, indicating a lack of reactive sites for the ALD precursors compared to growth on the SiO_2 surface, which exhibits no apparent inhibition.[4,5] On the other hand, nucleation on the PTCDA-functionalized surface is more efficient with growth progressing in a linear fashion following only 1−2 ALD cycles. Similar behavior is seen in Figure 4b, where the HfO_2 ALD on the bare EG is suppressed for ~7−8 cycles compared to the prompt nucleation on the SiO_2 surface, while the PTCDA functionalization reduces the nucleation period on EG to only 3−4 cycles. Since linear growth is typical of ALD on surfaces with a high concentration of reactive sites,[23] the ellipsometric data provide further evidence that PTCDA chemically functionalizes EG to facilitate chemisorption of the ALD Al_2O_3 and HfO_2 precursors.

To verify the chemical identity of the ALD dielectric films, XPS was performed on both the Al_2O_3- and HfO_2-coated PTCDA/EG samples (Figure 4c,d, respectively). Following survey scans to check for the presence of Al or Hf, high-resolution spectra of the Al 2p peak and the Hf 4f peaks were taken on the respective samples and calibrated relative to the C 1s peak. The Al 2p peak binding energy position at ~74.2 eV confirms the presence of Al_2O_3 (Figure 4c), while the Hf $4f_{7/2}$ peak binding energy position at ~16.5 eV confirms the presence of HfO_2 (Figure 4d).

X-ray Reflectivity of ALD Dielectric Films and Underlying PTCDA/EG. Specular X-ray reflectivity (XRR)[24−28] was used to confirm the integrity of the buried PTCDA/EG/SiC layers following ALD. This technique, while largely insensitive to the amorphous dielectric overlayer at high incident angles, probes the atomic-scale ordering of periodic surface and interface structures. In particular, synchrotron-based high-resolution XRR has been previously utilized in structurally probing both EG overlayers[27,29] and PTCDA-functionalized EG.[28] Additional analysis concentrating on the low-angle region of the XRR curves, which is sensitive to the thicker amorphous dielectric overlayers, was used to investigate

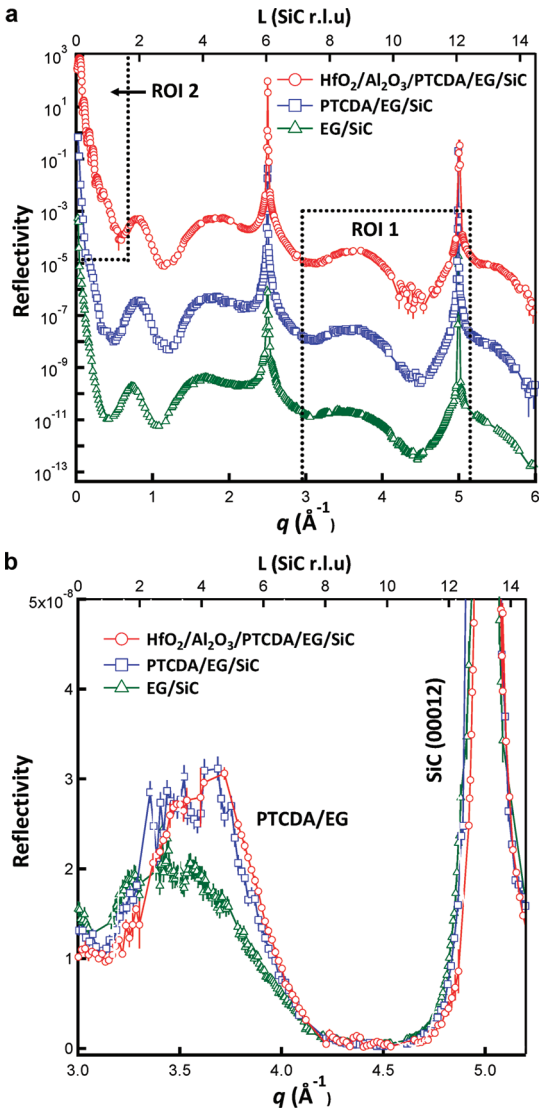

Figure 5. (a) XRR of EG/SiC(0001) (green), PTCDA/EG/SiC (blue), and HfO_2/Al_2O_3/PTCDA/EG/SiC (red). Sharp features at $q \sim 2.49$ and 4.99 $Å^{-1}$ correspond to the (0006) and (000 12) bulk SiC Bragg peaks, while the broad peaks at $q \sim 1.70$, 3.60, and 5.55 $Å^{-1}$ correspond to graphene and PTCDA overlayers. (b) In the first region of interest (ROI 1), the PTCDA/EG/SiC data exhibit a greater reflected intensity at $q \sim 3.60$ $Å^{-1}$ compared to that of bare EG/SiC. This feature is a result of the additional PTCDA monolayer and remains in the data after ALD deposition on the PTCDA-functionalized graphene surface (HfO_2/Al_2O_3/PTCDA/EG/SiC), indicating persistent interlayer structure following ALD.

the thickness, density, and roughness of the dielectric films.

Figure 5a displays specular XRR curves of three samples: bare EG/SiC, PTCDA/EG/SiC, and HfO_2(10 nm)/Al_2O_3(3 nm)/PTCDA/EG/SiC. The data are presented as a function of the modulus of the momentum transfer vector $q = 4\pi \sin(2\theta/2)/\lambda$, where 2θ is the scattering angle and λ is the X-ray wavelength. Allowed bulk SiC (0006) and (000 12) peaks can be seen at $q \sim 2.49$ and 4.99 $Å^{-1}$. Due to the similar interplanar spacings (~3.4 Å) of both graphene–graphene layers and

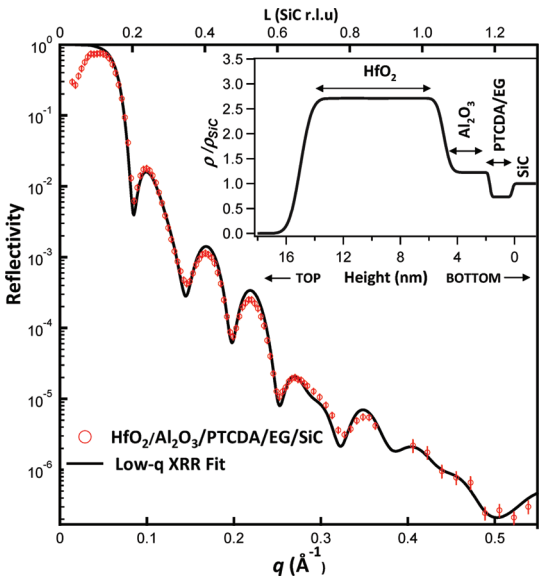

Figure 6. Low-q XRR is shown for the second region of interest (ROI 2) from Figure 5a. Kiessig fringes are observed, corresponding to a smooth, uniform dielectric film with sharp interfaces. The inset is the best least-squares fit result for the film overlayer strictly from the low-q data, with the electron density normalized to that of the bulk SiC substrate.

PTCDA–graphene layers,[28] the diffracted signals from these layers appear near the same positions along the XRR curve, at $q \sim 1.70$, 3.60, and 5.55 $Å^{-1}$. These features are present in all three data sets. As PTCDA and graphene layers have been shown to have similar stacking positions, the signal from either graphene or PTCDA/EG layers will be defined in this work as a generalized "interlayer". In addition to the high-q film signals, a broad thin-film oscillation can be observed in each data set with minima near $q = 0.40$ and 1.05 $Å^{-1}$. The positions of these minima imply an oscillation period Δq of 0.65 $Å^{-1}$, resulting from the PTCDA/EG interlayer structure of ~1 nm in thickness.[28]

Systematic changes in the XRR data due to the PTCDA functionalization of graphene have been described elsewhere.[28] Here, we note specifically that an increase in the reflected intensity near the interlayer peaks (at $q \sim 1.70$, 3.60, and 5.55 $Å^{-1}$) indicates the presence of a PTCDA overlayer. For clarity, in Figure 5b, all three data sets have been presented on a linear scale in the first region of interest (ROI 1) near the second-order interlayer peak. It is clear that the reflectivity from the bare EG/SiC sample differs from the other two PTCDA-functionalized samples. On the other hand, the PTCDA/EG/SiC and the HfO_2/Al_2O_3/PTCDA/EG/SiC data are nearly identical in this region, as well as along the rest of the XRR curve, excluding the very low-q region where Kiessig fringes from the dielectric film are evident. The agreement between the XRR spectra for the two PTCDA-functionalized samples indicates that the PTCDA remains intact in terms of layer occupation and stacking position

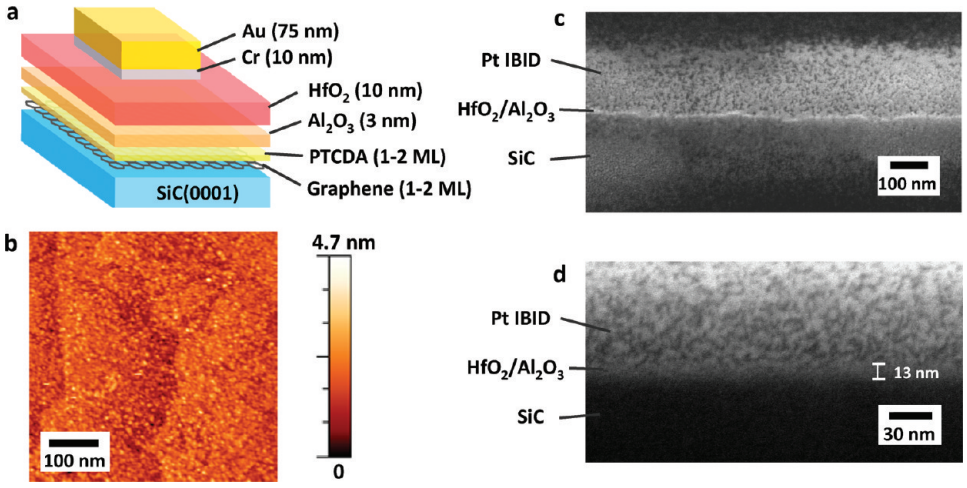

Figure 7. (a) Schematic of the metal-oxide-graphene parallel-plate capacitor structure with a 10 nm HfO_2 and 3 nm Al_2O_3 dielectric stack on a PTCDA-functionalized EG surface. (b) AFM image of the top surface after deposition of the dielectric stack. The underlying terraces of the substrate remain visible even following deposition of a 13 nm thick dielectric film. Cross-sectional SEM images of the dielectric layer taken at (c) a high beam current at 100 000× magnification and (d) a low beam current at 250 000× magnification. The dielectric stack thickness is measured to be ~13 nm thick as expected. Pt was deposited by IBID to allow for a smooth cross section during FIB milling.

relative to the underlying graphene following ALD of the high-*k* dielectric film.

In Figure 6, we investigate the low-*q* XRR data, denoted by ROI 2 in Figure 5a. The oscillations in the HfO_2/Al_2O_3/PTCDA/EG/SiC data reveal the presence of a smooth, uniform thin-film overlayer that is attributed to the dielectric thin-film stack. The final χ^2 value was 3.98.[30] The results of the fitting are displayed as an electron density profile in the inset of Figure 6.

Least-squares fitting[31] of the reflectivity data yielded a total dielectric film overlayer of thickness t_{tot} = 13.0 ± 0.4 nm, with a HfO_2 thickness of t_{HfO_2} = 10.0 ± 0.2 nm and a Al_2O_3 thickness of $t_{Al_2O_3}$ = 3.0 ± 0.2 nm, which is in close agreement with the thicknesses deduced from the ellipsometric data. The model provides for a low-density PTCDA/EG interface region, which the fit gave to be a 1.5 ± 0.2 nm thick layer. This thickness is consistent with previous work that indicates that the PTCDA/EG layer combined with the underlying $(6\sqrt{3} \times 6\sqrt{3})R30°$ SiC reconstructed layer is ~1.6 nm thick.[28] Extracted electron densities (reported with respect to the SiC substrate, ρ/ρ_{SiC}) are found to be ρ_{HfO_2}/ρ_{SiC} = 2.57 ± 0.04 and $\rho_{Al_2O_3}/\rho_{SiC}$ = 1.18 ± 0.04, in agreement with expected values derived from bulk crystal structures, which are nominally 2.50 for ρ_{HfO_2}/ρ_{SiC} and 1.18 for $\rho_{Al_2O_3}/\rho_{SiC}$. Additionally, the PTCDA/EG interlayer electron density ($\rho_{PTCDA/EG}/\rho_{SiC}$ = 0.71 ± 0.03) is close to the nominal value for a graphite crystal ($\rho_{graphite}/\rho_{SiC}$ = 0.65), reflecting the similarity between the two structures.[28] Extracted XRR rms roughnesses, which take into account both topography and density fluctuations, indicate exceptionally smooth surfaces and interfaces ($\sigma_{HfO_2,Air}$ = 0.60 ± 0.05 nm, $\sigma_{Al_2O_3,HfO_2}$ = 0.40 ± 0.05 nm, and $\sigma_{PTCDA/EG,Al_2O_3}$ = 0.2 ± 0.2 nm). The $\sigma_{HfO_2,Air}$= 0.60 ± 0.05 nm value obtained from the XRR measurements is in reasonably good agreement with the value $\sigma_{HfO_2,Air}$ ~ 0.3 nm measured by AFM given the finite AFM tip size. Overall, the low-*q* XRR indicates that the HfO_2 and Al_2O_3 dielectric layers grown on PTCDA/EG are smooth, uniform, and highly ordered. Furthermore, the high-angle XRR confirms that the buried PTCDA/EG layer remains structurally intact following ALD deposition.

Electrical Characterization of Metal-Oxide-Graphene Capacitors. In field-effect transistors (FETs), it is highly desirable to avoid power losses through gate leakage while maintaining the high capacitance necessary for low-voltage device operation. Since metal-oxide-semiconductor (MOS) capacitors provide a rapid assessment of gate dielectric quality in MOSFET technology,[32−35] we fabricated and characterized metal-oxide-graphene parallel-plate capacitors using ALD dielectrics grown on the PTCDA seeding layer. In particular, after SiC graphitization and deposition of PTCDA, 2 nm of ALD Al_2O_3 was deposited at a low growth temperature of 100 °C to avoid PTCDA desorption. The ALD growth temperature was then increased to 225 °C, whereupon another 1 nm of Al_2O_3 was deposited followed by 10 nm of HfO_2. The higher deposition temperature was employed to increase film density and improve dielectric quality.[29,36] Figure 7b is an AFM image of the top surface following ALD of the both Al_2O_3 and HfO_2 layers. The underlying terraces of the substrate are still observable even following 13 nm of ALD, showing that the total dielectric film is conformal, smooth, and homogeneous.

Cross-sectional scanning electron microscopy (SEM) images were taken using focused ion beam (FIB) milling in a dual beam FIB/SEM (FEI Helios Nanolab) to cut a trench into the dielectric stack to reveal its

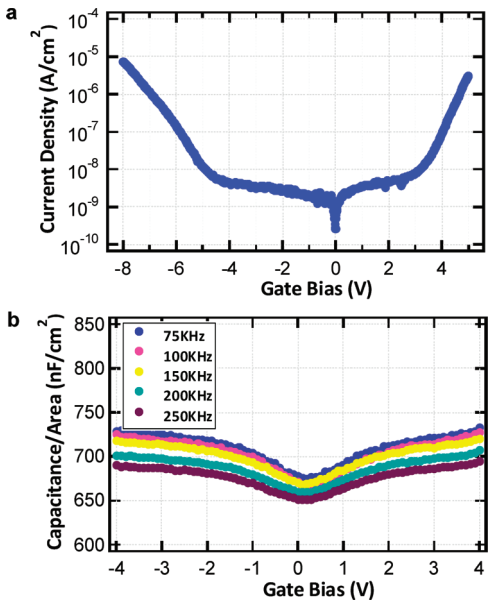

Figure 8. (a) Current–voltage characterization and (b) capacitance–voltage characterization of the dielectric stack (10 nm HfO_2, 3 nm Al_2O_3) grown on PTCDA-functionalized graphene.

cross-sectional structure. The FIB milling region was first prepared by depositing a thick layer of platinum *via* ion beam induced deposition (IBID), which allows for uniform cross-sectional FIB milling by minimizing charging effects. In the cross-sectional SEM image of Figure 7c, a bright layer is observed between the platinum IBID layer and the bulk SiC, which corresponds to the dielectric layers. The dielectric layers appear bright due to their electrically insulating properties, which causes negative charging and an increase in the secondary electron yield. Figure 7d was taken at a lower beam current to reduce this charging effect. In both cases, the dielectric layer is clearly visible with a measured thickness of 13 $\pm$ 3 nm as expected from the ALD growth conditions.

After ALD of the dielectric stack on PTCDA/EG, a Au (75 nm) on Cr (10 nm) top electrode layer was thermally evaporated (Nano38, Leskar) on the substrate through a TEM grid (90 μm hole width, SPI) to form a grid of square electrodes. The heavily doped SiC substrate (resistivity $\sim$0.054 $\Omega\cdot$cm) was used as the global bottom electrode. A schematic of the thin-film capacitor structure is shown in Figure 7a. At 1 V applied bias, low leakage currents of $\sim 5 \times 10^{-9}$ A/cm^2 were recorded for greater than 80% of the capacitors tested. At high biases exceeding 3 V, Fowler–Nordheim (FN) tunneling was observed as expected (Figure 8a). Irreversible dielectric breakdown was not observed up to a bias of 5 V, corresponding to an electric field of $\sim$4 MV/cm.

Capacitance–voltage (CV) measurements were performed over a frequency range of 10 kHz to 1 MHz (Figure 8b). The slight V-shape of the CV curves are similar to CV results obtained on exfoliated graphene on SiO_2[37,38] and epitaxial graphene on SiC,[39] which has been attributed to the influence from the quantum capacitance of graphene.[37–39] Capacitance dispersion with frequency is also observed, which likely results from the series substrate resistance and finite leakage current.[40,41] Using the two-frequency measurement technique[40] to account for this dispersion, a total capacitance of $\sim$700 nF/cm^2 was calculated across the dielectric stack. Bidirectional bias sweeps revealed minimal hysteresis of 0.1–0.4 V for the range of frequencies tested, which suggests low interface trap density. In addition, no differences were observed in the CV data taken in the light and in the dark. This measured capacitance is significantly higher than reported for previously published top-gated FETs on graphene,[10,14–16,42,43] while the measured gate leakage is significantly lower than reported values.[10,44] An exception is a recently published top-gate dielectric capacitance of 1200 nF/cm,[45] although the measured gate leakage of our dielectric stack is at least 4 orders of magnitude lower.

By assuming a parallel-plate capacitor geometry, dielectric constants for the ALD layers can be extracted using $k = Cd/\varepsilon_o$, where C is the capacitance per unit area, d is thickness of the film, and ε_o is the permittivity of free space. With this model, our capacitance measurements imply dielectric constants of 13 for HfO_2 (10 nm) and 5.6 for Al_2O_3 (3 nm), which are both consistent with previous reports[10,15] and similar to our measurements on reference silicon samples. Overall, the metal-oxide-graphene capacitor characteristics demonstrate the superlative dielectric properties of the PTCDA-seeded ALD dielectric films.

CONCLUSIONS

In summary, we have demonstrated the utility of vacuum sublimated organic monolayers of PTCDA as a seeding layer for ALD dielectric growth on epitaxial graphene on SiC(0001). Using a suite of surface science techniques including UHV STM, AFM, ellipsometry, XPS, XRR, and FIB-SEM, thin films of Al_2O_3 and HfO_2 grown on PTCDA/EG have been thoroughly characterized and shown to be exceptionally uniform, smooth, and conformal. In particular, with its subsurface sensitivity, XRR verifies that the underlying graphene remains intact and possesses sharp interfaces with the deposited dielectric films following ALD. To verify electrical integrity, metal-oxide-graphene parallel-plate capacitors were fabricated and shown to possess desirable characteristics including high capacitance values of $\sim$700 nF/cm^2 and low leakage currents of $\sim 5 \times 10^{-9}$ A/cm^2 at 1 V gate bias. This demonstration of high-k dielectric performance

shows the viability of organic self-assembled monolayers as seeding layers for ALD, thus providing a promising pathway for realizing high-performance graphene-based nanoelectronics.

METHODS

Sample Preparation: Epitaxial Graphene. The epitaxial graphene samples were grown on n-type (nitrogen-doped) 6H-SiC(0001) wafers (Cree, Inc.). The SiC wafer was diced into 9 mm × 6 mm sample pieces (American Precision Dicing), which were ultrasonically cleaned in acetone and isopropyl alcohol before being introduced into the UHV chamber (base pressure $\sim 5 \times 10^{-11}$ Torr). The samples were then outgassed at 600 °C overnight and annealed at 1100 °C for several minutes to remove the native oxide and other contaminants. The samples were subsequently graphitized by repeatedly heating to 1350 °C for 1 min cycles to produce a mixture of single-layer and bilayer graphene. The cleanliness of the surfaces and the graphene coverage were verified by room temperature STM imaging in the same UHV system.

Sample Preparation: PTCDA Monolayer. The PTCDA powder (97% purity, Sigma Aldrich) was loaded into an alumina-coated W boat and thoroughly outgassed in vacuum by resistively heating the boat. The PTCDA was deposited onto the EG substrates, which were held at room temperature, by thermal evaporation from the boat. The PTCDA monolayer coverage was verified by STM imaging and controlled by varying the duration of the molecular flux.

Sample Preparation: Atomic Layer Deposition. After deposition of PTCDA, the samples were briefly exposed to air, while being transferred to a separate custom viscous flow reactor for ALD.[23] Ultrahigh purity nitrogen was continuously passed through the flow tube at a rate of 360 sccm and a pressure of ~1 Torr. Al_2O_3 and HfO_2 films were prepared using trimethyl aluminum (TMA, Aldrich, 99%) and tetrakis(diethylamido)hafnium(IV) (TDEAHf, Aldrich, 99.99%), respectively. Deionized H_2O was used as the oxygen source in both cases. The TDEAHf vapor was delivered by a 60 sccm N_2 flow through a bubbler held at 120 °C.

Atomic Force Microscopy. All AFM images were collected utilizing a modified CP Research (Thermomicroscopes) AFM in air. Imaging was performed in intermittent contact mode using a Si probe (μMasch, NSC36A) with a nominal tip radius of curvature of 10 nm. AFM images were rendered using WSxM SPM analysis software.[46]

Current mapping was achieved with a conductive diamond-coated Si probe (CDT-FMR, Nanosensors) in contact mode with contact forces of 8−50 nN, scan rate of 0.3 Hz, and sample bias of 0.3 V. Current was collected through the conductive AFM probe using a DL Instruments current preamplifier (model 1212) and a 160 Hz low-pass in-line filter. A limiting resistor (~12 MΩ) was used in series with the current preamplifier to prevent exposure of the conductive AFM tip to potentially damagingly high current levels. The conductive AFM probes were tested on Au reference samples, where contact resistances of <5 kΩ were recorded. Contact-mode topography signals were collected concurrently with the current signal.

Ellipsometry. Ellipsometric measurements were performed using a J.A. Woolam Co. M2000 V variable angle spectroscopic ellipsometer (VASE) at an incidence angle of 75°. Measurements were obtained before and after ALD. Nominal thicknesses of Al_2O_3 and HfO_2 dielectric films were found by fitting the spectra to a model using optical constants of the dielectric films and the contribution from the substrate obtained preceding ALD.

X-ray Photoelectron Spectroscopy. An Omicron ESCA (Electron Spectroscopy for Chemical Analysis) probe was used for XPS analysis. The measurements were made using Al Kα (1486.6 eV) radiation, which was incident on the sample at a 45° takeoff angle, and a hemispherical electron energy analyzer. A survey scan was initially performed to check for the presence of Al and Hf peaks after Al_2O_3 and HfO_2 ALD, respectively. Subsequently, high-resolution spectra of the Al 2p peak and the Hf 4f peaks were gathered on the respective samples and calibrated relative to the C 1s peak.

X-ray Reflectivity. Specular X-ray reflectivity was measured at beamline 33-BM-C of the X-ray Operation and Research Division, Advanced Photon Source (APS), Argonne National Laboratory. The incident photon beam on the sample had an energy of 17.00 keV, beam size of 0.1 mm (vertical) × 2.00 mm (horizontal), and incident flux of $\sim 10^{10}$ photons/s. Samples were mounted within an evacuated ($\sim 10^{-3}$ Torr) beryllium dome sample cell. The scattered X-ray intensity in the region of the specular condition was acquired with either a point detector (low-angle reflectivity; $0 < q < 1.25$ Å^{-1})[47] or with a 2D CCD detector ($q > 1.00$ Å^{-1}).[24] Data from these two methods were combined to produce a single XRR curve with overlapping regions between $q = 1.00$ and 1.25 Å^{-1}. Uncertainties for all data points were determined by counting statistics. For simplification of reflectivity analysis, data points were removed near the sharp quasi-forbidden SiC(000 L) Bragg peaks[27,48] at $q = 2\pi n/c_{lat}$, where n is an integer value that is not a multiple of 6 and c_{lat} = 15.12 Å is the 6H-SiC(0001) out-of-plane lattice parameter.

Low-q reflectivity for the HfO_2/Al_2O_3/PTCDA/EG/SiC was fit between $q = 0.08$ and 0.6 Å^{-1} using the Motofit[31] package in the Igor Pro environment. Theoretical reflectivity curves were calculated using the Abeles matrix method and were fit utilizing both Genetic Optimization and Levenberg−Marquardt minimization algorithms. The model included 3 ($n = 1-3$) overlayers (a PTCDA/EG layer, an Al_2O_3 layer, and a HfO_2 layer) and allowed 3 free parameters per layer (electron density, ρ_n, rms interface roughness, $\sigma_{n,n+1}$, and layer thickness, t_n). In addition to these parameters, the roughness of the SiC was allowed to vary while the bulk density was fixed, resulting in a total of 10 free parameters.

FIB/SEM Characterization. Cross-sectional scanning electron microscopy (SEM) images were taken using focused ion beam (FIB) milling in a dual beam FIB/SEM (FEI Helios Nanolab). The FIB milling region was first prepared by depositing a thick layer of platinum *via* ion beam induced deposition (IBID). A trench was then FIB milled to allow for SEM access to the cross section of the dielectric film. Finally, SEM images were taken at a 38° angle to the normal of the cross section, causing an apparent contraction of the vertical scale by a factor of 0.788.

Electrical Characterization. After ALD, a top electrode layer of Au (75 nm) on Cr (10 nm) was thermally evaporated (Nano38, Leskar) on the substrate through a TEM grid (90 μm hole width, SPI) to form a grid of square electrodes, the size of which was measured by an optical microscope (ME600, Nikon). The highly doped SiC substrate (resistivity ~0.054 Ω·cm) was used as the global bottom electrode. All electrical measurements were performed under ambient conditions. Contact to the top electrode was made with a conductive diamond-coated Si probe (CDT-FMR, Nanosensors) that was actuated by an AFM. Contact forces were held at ~0.5 μN to maintain good electrical contact. Current−voltage measurements were performed with a Keithley 2636A dual source meter, and capacitance−voltage curves were gathered with an HP 4192A impedance analyzer.

Acknowledgment. This work was supported by the National Science Foundation (Award Number DMR-0520513), the Office of Naval Research (Award Number N00014-09-1-0180), Argonne National Laboratory (ANL), and ANSER Energy Frontier Research Center (funded by the Department of Energy, Award Number DE-SC0001059). ANL is a U.S. Department of Energy Office of Science Laboratory operated under Contract No. DE-AC02-06CH11357 by UChicago Argonne, LLC. In addition, the FIB-SEM characterization by A.L.L. was funded by the Department of Energy (Award Number DE-AC02-06CH11357 to the CEES-

EFRC). FIB-SEM and XPS were performed in the NUANCE facility at Northwestern University, which is supported by the NSF-NSEC, NSF-MRSEC, Keck Foundation, and State of Illinois. The authors thank P. Fenter for the development of extraction and analysis routines for the XRR data. Finally, the authors acknowledge J. Lyding for use of his STM control software.

REFERENCES AND NOTES

1. Castro Neto, A. H.; Guinea, F.; Peres, N. M. R.; Novoselov, K. S.; Geim, A. K. The Electronic Properties of Graphene. *Rev. Mod. Phys.* **2009**, *81*, 109–162.
2. Geim, A. K. Graphene: Status and Prospects. *Science* **2009**, *324*, 1530–1534.
3. Bolotin, K. I.; Sikes, K. J.; Jiang, Z.; Klima, M.; Fudenberg, G.; Hone, J.; Kim, P.; Stormer, H. L. Ultrahigh Electron Mobility in Suspended Graphene. *Solid State Commun.* **2008**, *146*, 351–355.
4. Wang, X. R.; Tabakman, S. M.; Dai, H. J. Atomic Layer Deposition of Metal Oxides on Pristine and Functionalized Graphene. *J. Am. Chem. Soc.* **2008**, *130*, 8152–8153.
5. Xuan, Y.; Wu, Y. Q.; Shen, T.; Qi, M.; Capano, M. A.; Cooper, J. A.; Ye, P. D. Atomic-Layer-Deposited Nanostructures for Graphene-Based Nanoelectronics. *Appl. Phys. Lett.* **2008**, *92*, 013101.
6. Shen, T.; Gu, J. J.; Xu, M.; Wu, Y. Q.; Bolen, M. L.; Capano, M. A.; Engel, L. W.; Ye, P. D. Observation of Quantum-Hall Effect in Gated Epitaxial Graphene Grown on SiC(0001). *Appl. Phys. Lett.* **2009**, *95*, 172105.
7. Chen, Q.; Huang, H.; Chen, W.; Wee, A. T. S.; Feng, Y. P.; Chai, J. W.; Zhang, Z.; Pan, J. S.; Wang, S. J. *In Situ* Photoemission Spectroscopy Study on Formation of HfO_2 Dielectrics on Epitaxial Graphene on SiC Substrate. *Appl. Phys. Lett.* **2010**, *96*, 072111.
8. Robinson, J. A.; LaBella, M.; Trumbull, K. A.; Weng, X. J.; Cavelero, R.; Daniels, T.; Hughes, Z.; Hollander, M.; Fanton, M.; Snyder, D. Epitaxial Graphene Materials Integration: Effects of Dielectric Overlayers on Structural and Electronic Properties. *ACS Nano* **2010**, *4*, 2667–2672.
9. Pirkle, A.; Wallace, R. M.; Colombo, L. *In Situ* Studies of Al_2O_3 and HfO_2 Dielectrics on Graphite. *Appl. Phys. Lett.* **2009**, *95*, 133106.
10. Kim, S.; Nah, J.; Jo, I.; Shahrjerdi, D.; Colombo, L.; Yao, Z.; Tutuc, E.; Banerjee, S. K. Realization of a High Mobility Dual-Gated Graphene Field-Effect Transistor with Al_2O_3 Dielectric. *Appl. Phys. Lett.* **2009**, *94*, 062107.
11. Pirkle, A.; Chabal, Y. J.; Colombo, L.; Wallace, R. M. *In-Situ* Studies of High-κ Dielectrics for Graphene-Based Devices. *ECS Trans.* **2009**, *19*, 215–224.
12. Lee, B. K.; Park, S. Y.; Kim, H. C.; Cho, K.; Vogel, E. M.; Kim, M. J.; Wallace, R. M.; Kim, J. Y. Conformal Al_2O_3 Dielectric Layer Deposited by Atomic Layer Deposition for Graphene-Based Nanoelectronics. *Appl. Phys. Lett.* **2008**, *92*, 203102.
13. Lee, B.; Mordi, G.; Kim, M. J.; Chabal, Y. J.; Vogel, E. M.; Wallace, R. M.; Cho, K. J.; Colombo, L.; Kim, J. Characteristics of High-k Al_2O_3 Dielectric Using Ozone-Based Atomic Layer Deposition for Dual-Gated Graphene Devices. *Appl. Phys. Lett.* **2010**, *97*, 043107.
14. Lin, Y. M.; Jenkins, K. A.; Valdes-Garcia, A.; Small, J. P.; Farmer, D. B.; Avouris, P. Operation of Graphene Transistors at Gigahertz Frequencies. *Nano Lett.* **2009**, *9*, 422–426.
15. Farmer, D. B.; Chiu, H. Y.; Lin, Y. M.; Jenkins, K. A.; Xia, F. N.; Avouris, P. Utilization of a Buffered Dielectric To Achieve High Field-Effect Carrier Mobility in Graphene Transistors. *Nano Lett.* **2009**, *9*, 4474–4478.
16. Lin, Y. M.; Dimitrakopoulos, C.; Jenkins, K. A.; Farmer, D. B.; Chiu, H. Y.; Grill, A.; Avouris, P. 100-GHz Transistors from Wafer-Scale Epitaxial Graphene. *Science* **2010**, *327*, 662–662.
17. Liao, L.; Duan, X. Graphene-Dielectric Integration for Graphene Transistors. *Mater. Sci. Eng., R* **2010**, *70*, 354–370.
18. Wang, Q. H.; Hersam, M. C. Room-Temperature Molecular-Resolution Characterization of Self-Assembled Organic Monolayers on Epitaxial Graphene. *Nat. Chem.* **2009**, *1*, 206–211.
19. Huang, H.; Chen, S.; Gao, X. Y.; Chen, W.; Wee, A. T. S. Structural and Electronic Properties of PTCDA Thin Films on Epitaxial Graphene. *ACS Nano* **2009**, *3*, 3431–3436.
20. Kellar, J. A.; Alaboson, J. M. P.; Wang, Q. H.; Hersam, M. C. Identifying and Characterizing Epitaxial Graphene Domains on Partially Graphitized SiC(0001) Surfaces Using Scanning Probe Microscopy. *Appl. Phys. Lett.* **2010**, *96*, 143103.
21. Alaboson, J. M. P.; Wang, Q. H.; Kellar, J. A.; Park, J.; Elam, J. W.; Pellin, M. J.; Hersam, M. C. Conductive Atomic Force Microscope Nanopatterning of Epitaxial Graphene on SiC(0001) in Ambient Conditions. *Adv. Mater.* **2011**, *23*, 2181–2184.
22. Foley, E. T.; Yoder, N. L.; Guisinger, N. P.; Hersam, M. C. Cryogenic Variable Temperature Ultra-high Vacuum Scanning Tunneling Microscope for Single Molecule Studies on Silicon Surfaces. *Rev. Sci. Instrum.* **2004**, *75*, 5280–5287.
23. Elam, J. W.; Groner, M. D.; George, S. M. Viscous Flow Reactor with Quartz Crystal Microbalance for Thin Film Growth by Atomic Layer Deposition. *Rev. Sci. Instrum.* **2002**, *73*, 2981–2987.
24. Fenter, P.; Catalano, J. G.; Park, C.; Zhang, Z. On the Use of CCD Area Detectors for High-Resolution Specular X-ray Reflectivity. *J. Synchrotron Radiat.* **2006**, *13*, 293–303.
25. Fenter, P. A. X-ray Reflectivity as a Probe of Mineral−Fluid Interfaces: A User Guide. *Rev. Mineral Geochem.* **2002**, *49*, 149–220.
26. Robinson, I. K.; Tweet, D. J. Surface X-ray-Diffraction. *Rep. Prog. Phys.* **1992**, *55*, 599–651.
27. Hass, J.; Millan-Otoya, J. E.; First, P. N.; Conrad, E. H. Interface Structure of Epitaxial Graphene Grown on 4h-SiC(0001). *Phys. Rev. B* **2008**, *78*, 205424.
28. Emery, J. D.; Wang, Q. H.; Zarrouati, M.; Fenter, P.; Hersam, M. C.; Bedzyk, M. J. Structural Analysis of PTCDA Layers on Epitaxial Graphene with High-Resolution X-ray Reflectivity. *Surf. Sci.* 2010, DOI: 10.1016/j.susc.2010.11.008.
29. Hass, J.; Feng, R.; Millan-Otoya, J. E.; Li, X.; Sprinkle, M.; First, P. N.; de Heer, W. A.; Conrad, E. H.; Berger, C. Structural Properties of the Multilayer Graphene/4H-SiC(000$\bar{1}$) System As Determined by Surface X-ray Diffraction. *Phys. Rev. B* **2007**, *75*, 214109.
30. Here, $\chi^2 = [I_k(I_k - I_{calc,k})^2/\sigma_k{}^2]/(N - N_p)$, where I_k and $I_{calc,k}$ are the measured and calculated reflected intensities, respectively, σ_k is the measured uncertainty at the kth data point, and N and N_p are the number of data points and parameters used in the fit, respectively.
31. Nelson, A. Co-refinement of Multiple-Contrast Neutron/X-ray Reflectivity Data Using MOTOFIT. *J. Appl. Crystallogr.* **2006**, *39*, 273–276.
32. Groner, M. D.; Elam, J. W.; Fabreguette, F. H.; George, S. M. Electrical Characterization of Thin Al_2O_3 Films Grown by Atomic Layer Deposition on Silicon and Various Metal Substrates. *Thin Solid Films* **2002**, *413*, 186–197.
33. Chen, H. W.; Chiu, F. C.; Liu, C. H.; Chen, S. Y.; Huang, H. S.; Juan, P. C.; Hwang, L. Interface Characterization and Current Conduction in HfO_2-Gated MOS Capacitors. *Appl. Surf. Sci.* **2008**, *254*, 6112–6115.
34. Cheng, J. Y.; Huang, C. T.; Hwu, J. G. Comprehensive Study on the Deep Depletion Capacitance−Voltage Behavior for Metal-Oxide-Semiconductor Capacitor with Ultrathin Oxides. *J. Appl. Phys.* **2009**, *106*, 074507.
35. Shahrjerdi, D.; Garcia-Gutierrez, D. I.; Akyol, T.; Bank, S. R.; Tutuc, E.; Lee, J. C.; Banerjee, S. K. GaAs Metal-Oxide-Semiconductor Capacitors Using Atomic Layer Deposition of HfO_2 Gate Dielectric: Fabrication and Characterization. *Appl. Phys. Lett.* **2007**, *91*, 193503.
36. Hausmann, D. M.; Kim, E.; Becker, J.; Gordon, R. G. Atomic Layer Deposition of Hafnium and Zirconium Oxides Using Metal Amide Precursors. *Chem. Mater.* **2002**, *14*, 4350–4358.
37. Xia, J. L.; Chen, F.; Li, J. H.; Tao, N. J. Measurement of the Quantum Capacitance of Graphene. *Nat. Nanotechnol.* **2009**, *4*, 505–509.

38. Chen, Z.; Appenzeller, J. Mobility Extraction and Quantum Capacitance Impact in High Performance Graphene Field-Effect Transistor Devices. *IEEE IEDM Tech. Digest.* **2008**, *21.1*, 509–512.
39. Xia, J. L.; Chen, F.; Tedesco, J. L.; Gaskill, D. K.; Myers-Ward, R. L.; Eddy, C. R.; Ferry, D. K.; Tao, N. J. The Transport and Quantum Capacitance Properties of Epitaxial Graphene. *Appl. Phys. Lett.* **2010**, *96*, 162101.
40. Yang, K. J.; Hu, C. MOS Capacitance Measurements for High-Leakage Thin Dielectrics. *IEEE Trans. Electron Devices* **1999**, *46*, 1500–1501.
41. Lu, Y.; Hall, S.; Tan, L. Z.; Mitrovic, I. Z.; Davey, W. M.; Raeissi, B.; Engstrom, O.; Cherkaoui, K.; Monaghan, S.; Hurley, P. K.; *et al.* Leakage Current Effects on C−V Plots of High-k Metal-Oxide-Semiconductor Capacitors. *J. Vac. Sci. Technol., B* **2009**, *27*, 352–355.
42. Xia, F. N.; Farmer, D. B.; Lin, Y. M.; Avouris, P. Graphene Field-Effect Transistors with High On/Off Current Ratio and Large Transport Band Gap at Room Temperature. *Nano Lett.* **2010**, *10*, 715–718.
43. Szafranek, B. N.; Schall, D.; Otto, M.; Neumaier, D.; Kurz, H. Electrical Observation of a Tunable Band Gap in Bilayer Graphene Nanoribbons at Room Temperature. *Appl. Phys. Lett.* **2010**, *96*, 112103.
44. Wu, Y. Q.; Ye, P. D.; Capano, M. A.; Xuan, Y.; Sui, Y.; Qi, M.; Cooper, J. A.; Shen, T.; Pandey, D.; Prakash, G.; Reifenberger, R. Top-Gated Graphene Field-Effect-Transistors Formed by Decomposition of SiC. *Appl. Phys. Lett.* **2008**, *92*, 092102.
45. Wang, Z.; Xu, H.; Zhang, Z.; Wang, S.; Ding, L.; Q., Z.; Yang, L.; Pei, T.; Liang, X.; Gao, M.; Peng, L. Growth and Performance of Yttrium Oxide as an Ideal High-k Gate Dielectric for Carbon-Based Electronics. *Nano Lett.* **2010**, *10*, 2024–2030.
46. Horcas, I.; Fernandez, R.; Gomez-Rodriguez, J. M.; Colchero, J.; Gomez-Herrero, J.; Baro, A. M. WSXM: A Software for Scanning Probe Microscopy and a Tool for Nanotechnology. *Rev. Sci. Instrum.* **2007**, *78*, 013705.
47. Rauscher, M.; Reichert, H.; Engemann, S.; Dosch, H. Local Density Profiles in Thin Films and Multilayers from Diffuse X-ray and Neutron Scattering. *Phys. Rev. B* **2005**, *72*, 205401.
48. Bauer, A.; Reischauer, P.; Krausslich, J.; Schell, N.; Matz, W.; Goetz, K. Structure Refinement of the Silicon Carbide Polytypes 4h and 6h: Unambiguous Determination of the Refinement Parameters. *Acta Crystallogr. A* **2001**, *57*, 60–67.